

PCCP

Accepted Manuscript



This is an *Accepted Manuscript*, which has been through the Royal Society of Chemistry peer review process and has been accepted for publication.

Accepted Manuscripts are published online shortly after acceptance, before technical editing, formatting and proof reading. Using this free service, authors can make their results available to the community, in citable form, before we publish the edited article. We will replace this *Accepted Manuscript* with the edited and formatted *Advance Article* as soon as it is available.

You can find more information about *Accepted Manuscripts* in the [Information for Authors](#).

Please note that technical editing may introduce minor changes to the text and/or graphics, which may alter content. The journal's standard [Terms & Conditions](#) and the [Ethical guidelines](#) still apply. In no event shall the Royal Society of Chemistry be held responsible for any errors or omissions in this *Accepted Manuscript* or any consequences arising from the use of any information it contains.

How Tubular Aggregates Interact with Biomembranes: Wrapping, Fusion and Pearling†

Tongtao Yue,^{*a} Yan Xu,^a Mingbin Sun,^a Xianren Zhang^b and Fang Huang^{*a}

^a *State Key Laboratory of Heavy Oil Processing, Center for Bioengineering and Biotechnology, China University of Petroleum (East China), Qingdao, 266580, China.*

E-mail: yuettt@upc.edu.cn, fhuang@upc.edu.cn

^b *State Key Laboratory of Organic-Inorganic Composites, Beijing University of Chemical Technology, Beijing, 100029, China.*

† Electronic supplementary information (ESI) available: Video S1 for full wrapping dynamics of tube by membrane; Video S2 for tube pearling dynamics under increased inner water pressure and weak tube-membrane adhesion; Video S3 for membrane wrapping of one pearled tube; Figure S1 for detailed structure of membrane monolayer protrusion; Figure S2 for heterogeneous wrapping dynamics along tube axial direction; Figure S3 for promoted tube pearling by weak tube-membrane adhesion; Figure S4 for restrained tube pearling by strong tube-membrane adhesion; and Figure S5 for membrane wrapping of one pearled tube.

Abstract

How soft tubular aggregates interact with biomembranes is crucial for understanding the formation of membrane tubes connecting two eukaryotic cells, which are initially created from one cell and then connect with the other. On the other hand, recent experiments have shown that tubular polymersomes display different cellular internalization kinetics in their biomedical applications compared with spherical ones with an underlying mechanism that is not fully understood. Inspired by above observations, in this work we investigate how tubular aggregates interact with biomembranes with the aid of computer simulation techniques. We identify three different pathways for membrane interaction with parallel tubes: membrane wrapping, tube-membrane fusion and tube pearling. For the first pathway, soft tubes can be wrapped from the top side by membranes through membrane monolayer protrusion, which cooperatively leads to a heterogeneous wrapping dynamics along with the tube deformation. The second pathway found is that soft tubes fuse with the membrane under certain conditions. Both wrapping and fusion have distinct influences on the third pathway, tube pearling. While a weak membrane adhesion promotes tube pearling, the strong adhesion that leads to higher extent of membrane wrapping conversely restrains tube pearling. Under highly positive membrane tension, partial tube-membrane fusion provides another way to mediate tube pearling. The findings shed light on the formation of bridge membrane tube and the rational design of tube-based therapeutic agents with improved efficiency for targeted cellular delivery.

1. Introduction

Nowadays, biomedical applications of nanotechnology have received considerable attention.¹ In particular, various nanoparticles (NPs) have been intelligently and specifically designed for bioimaging, biosensing, diagnostics and therapeutics.²⁻⁴ For these applications, controlling the NP ability to facilitate their uptake by cells is particularly desirable via optimizing the physiochemical property of NPs.

In general, there are two common internalization pathways: direct translocation across the membrane and internalization via an endocytic pathway. It has been demonstrated that by controlling NP properties, like size,⁵⁻⁷ shape,⁸⁻¹³ elasticity¹⁴⁻¹⁸ and surface chemistry,¹⁹⁻²¹ it is possible to manipulate the endocytosis machinery and thus influence the internalization efficiency.^{22, 23} For NP size, there exists the optimal and minimum wrapping radius for successful endocytosis.^{5, 7} Exceedingly large NPs yield an inefficient uptake, while rather small NPs must aggregate and be wrapped by the membrane cooperatively.²⁴⁻²⁷ For the effect of NP shape, both local curvature and mean curvature are found to affect the endocytosis efficiency.^{12, 13} Besides, the membrane wrapping of NPs is affected by both passive and active NP rotation.²⁸⁻³¹ For mechanical property, both theoretical and simulation works have demonstrated that stiff NPs can be more easily wrapped by membrane than soft ones.^{14, 18}

Compared with traditional rigid NPs, soft vesicles or polymersomes offer particular advantages, like high solubility, high environmental sensitivity, biocompatibility and low toxicity.³²⁻³⁴ Besides, they can encapsulate hydrophobic molecules within the membrane, but unlike solid NPs, polymersomes are also capable of encapsulating a range of hydrophilic molecules within their lumen. Recently, Robertson *et al.* reported the formation of pH-sensitive tubular polymersomes from polymer film hydration,³⁵ indicating that the tubular polymersomes can encapsulate both hydrophobic and hydrophilic cargoes and deliver them into clinically relevant cells. More importantly, it was found that the internalization kinetics of polymersomes

is strongly influenced by their shape.

Since the great potential of soft biocompatible nanomaterials in cellular delivery, it becomes urgent to systematically understand their interaction with cell membranes. For tubular polymersomes, specially, how they interact with cell membrane remains largely unknown. On the other hand, this question is closely related to the biological function of membrane tubes, which play an essential role in intercellular material exchange and signal communication.³⁶ A fundamental question regarding the formation of membrane tube that connects two eukaryotic cells is how the membrane tubes interact with cell membrane when they meet. To answer these questions, we applied the Dissipative Particle Dynamics (DPD) simulation method to systematically investigate the pathway of membrane interaction with parallel tubes. We should note that in reality the initial contact between membrane and tube is diverse and more likely to be different than parallel. Here we simply considered parallel tube because the periodic boundary conditions were applied in all three directions. For long periodic tube, the only feasible way to investigate its interaction with membrane is placing it parallel with the membrane surface. Moreover, once tubular aggregate approaches the membrane with any orientation, the maximization of tube-membrane adhesion would force the tube to lie down before onset of subsequent interaction. The rapid rotation has been confirmed for anisotropic NPs adhering on membrane surface.^{10, 28}

2. Models and Simulation Methods

2.1 Models

The lipid molecule is represented by the HIT3 model, where H and T denote the hydrophilic lipid head and hydrophobic lipid tails, respectively. The HIT3 lipid model, which was first introduced to study the dynamics of phase separation in multi-component lipid vesicles,³⁷ can self assemble into planar, vesicular and tubular membranes. In this work, the tube is constructed by arranging 12000 lipid molecules in a defined cylindrical surface. To eliminate the effect of predefined initial configuration and balance the pressure difference between inside and outside of the

tube, the tube is first relaxed at a higher temperature of 2.0 for 50000 time steps, and then annealed slowly to a lower temperature of 1.0. After an equilibrium simulation of 100000 steps, the tube with diameter of $16.8 r_c$ and length of $70 r_c$ is closely placed on the surface of a pre-equilibrated membrane with lipid number of 26000. We can convert the DPD length unit to SI unit by mapping the membrane thickness. Specifically, the thickness of DPPC bilayer is experimentally measured to about 4 nm. In our simulations, the membrane thickness is about $3.2 r_c$. Thus we can yield $r_c = 1.25$ nm. The summary of system components used for simulations are given in Figure 1.

2.2 DPD Simulation method

The DPD method, which is a coarse-grained simulation technique with hydrodynamic interactions, was first introduced to simulate the hydrodynamic behavior of complex fluids.³⁸⁻⁴⁰ Recently, it has become one of the most commonly used computer simulation techniques to study the biomembrane system, especially on the interaction between membranes and NPs.⁴¹⁻⁴⁴ In DPD, the dynamics of each elementary unit is governed by Newton's equation of motion, $dr_i/dt=v_i$ and $dv_i/dt=f_i/m_i$, similar to the molecular dynamics simulation method. Typically, beads i and j interact with each other via a pairwise additive force consisting of a conservative force F_{ij}^C , a dissipative force F_{ij}^D and a random force F_{ij}^R . Thus, the total force exerted on bead i by bead j can be expressed as $F_i = \sum_{i \neq j} (F_{ij}^C + F_{ij}^D + F_{ij}^R)$.

The conservative force, which is soft and repulsive, is determined by $F_{ij}^C = a_{ij} \tilde{r}_{ij} \max\{1 - r_{ij}/r_c, 0\}$, where a_{ij} is the maximum repulsive force constant between beads i and j , $r_{ij} = r_j - r_i$ (r_i and r_j are their positions), $\tilde{r}_{ij} = |r_{ij}|/r_{ij}$, and r_c is the cut off radius. The value of a_{ij} is mainly determined according to the hydrophobicity of two interacting beads. For any two beads of the same type, we take the repulsive parameter $a_{ij} = 25$, and for any two beads of different types, we set the

interaction parameter to denote the hydrophilic/hydrophobic property of the beads as follows: $a_{ij} = 25$ if the two beads are both hydrophilic or hydrophobic, while $a_{ij} = 200$ if one is hydrophilic and the other is hydrophobic. In order to model the tube-membrane adhesion, we set the interaction parameter $a_{HrH_M} < 25$ and vary its value to regulate the tube-membrane adhesion strength. In most of our simulations, we set the interaction parameter $a_{T_T M} = 200$ to prevent the tube-membrane fusion. Although some atomic details are sacrificed in the coarse-grained DPD method, the essential features of the system are reproduced by the simulation model and the parameter set.⁴⁵

The dissipative force has the form $F_{ij}^D = -\gamma(1 - r_{ij}/r_c)^2(\tilde{r}_{ij} \cdot v_{ij})\tilde{r}_{ij}$, where γ is the friction coefficient, $v_{ij} = v_j - v_i$ (v_i and v_j are their velocities). This expression is chosen to conserve the momentum of each pair of beads, and thus the total momentum of the system is conserved.

The random force between beads i and j is calculated by $F_{ij}^R = -\sigma(1 - r_{ij}/r_c)^2\theta_{ij}\tilde{r}_{ij}$, where σ represents the noise amplitude, and θ_{ij} is an uncorrelated random variable with zero mean and unit variance.

In the model of lipid molecules, the interaction between neighboring beads within the same molecule is described by a harmonic spring force, which is given by $F_S = K_S(r_{ij} - r_{eq})\tilde{r}_{ij}$, where K_S and r_{eq} are the spring constant and the equilibrium bond length, respectively. The numerical values of K_S and r_{eq} used for our simulations are 128 and 0.7, respectively.

In order to maintain the bending rigidity of the lipids, the force constraining the variation of the bond angle is given by $F_\varphi = -\nabla U_\varphi$ and $U_\varphi = K_\varphi(1 - \cos(\varphi - \varphi_0))$, where $K_\varphi = 10.0$ and $\varphi_0 = \pi$ are the bond bending force constant and equilibrium bond angle, respectively.

In DPD simulations, we apply the Velocity Verlet integration algorithm and the

integration time step is $\Delta t = 0.02\tau$. The cutoff radius r_c , bead mass m and energy $k_B T$ are chosen as the simulation units. The periodic boundary conditions are adopted in all three directions. The simulation box size is $70 r_c \times 70 r_c \times 60 r_c$ with a number density of 3.

2.3 N-varied DPD Method

In this work, all simulations are performed in N-varied VT ensembles, in which the targeted membrane tension can be controlled by monitoring the lipid number per area (LNPA) in a boundary membrane region.⁴⁶ The boundary region, which locates on both sides of the tube, thus plays a role as the lipid reservoir (Fig. 1). By adding or deleting lipids, the value of LNPA in the boundary region is kept within a defined range ($\rho_{LNPA}^{\min} < \rho_{LNPA} < \rho_{LNPA}^{\max}$). In an addition move, a number of lipid molecules are inserted into the boundary region if the local lipid area density is less than ρ_{LNPA}^{\min} . Conversely, if the average area density of lipids in the boundary region exceeds ρ_{LNPA}^{\max} , a corresponding number of lipids are deleted randomly from the boundary region. In order to keep the whole density of the beads in the simulation box constant, a corresponding number of water beads are randomly added or deleted simultaneously. In practice, the addition or deletion move is performed every 1000 time steps in order to leave enough time to propagate the tension to the whole membrane.

3. Results and Discussion

Recent experimental observation suggested that tubular polymersomes display different cellular internalization kinetics compared to spherical ones.³⁵ One typical reason is that tubular polymersomes have anisotropic shapes. For soft spherical NPs, the membrane wrapping is generally accompanied by NP deformation,^{15,47} and thus depends on the bending rigidity ratio between NPs and membranes.¹⁴ For soft cylindrical tubes, pearling was observed under external interventions, such as polymer anchorage and electric field.⁴⁸ When soft tubes and membranes meet, the question

would become much more complicated. Unlike spherical elastic aggregates, the symmetry breaking of cylindrical tubes may cause heterogeneous deformation as they are wrapped by membranes. The heterogeneous deformation may make the cylindrical tubes unstable and lead to tube pearling. Motivated by above facts and consideration, in this work we performed extensive simulations, aiming to systematically understand the interaction pathway between cylindrical tubes and membranes.

3.1 Wrapping Pathway of Tubes by Membranes

Partial Wrapping. First, we considered the situation of weak tube-membrane adhesion. The interaction parameter $a_{H_T H_M}$ that represents the tube-membrane adhesion strength was set to 10.0. Our simulation suggests that under the condition of zero membrane tension ($\rho_{LNPA}=1.4$), the tube is only slightly wrapped by the membrane (Fig. 2A). In order to quantify the extent of tube deformation due to membrane adhesion, we calculated the tube ellipsoidal ratio, which is defined as $E = a/b$, with a and b being the height and width of the tube cross section, respectively (Fig. 2B). It is the adhesion that maximizes the tube-membrane contact area and induces the deformation of tube morphology. In particular, sharp local curvature change for the tube was observed near the three phase contact line between solvent-membrane interface and solvent-tube interface. Energetically, the final wrapping state is determined by competition of tube-membrane adhesion energy and membrane bending energy.^{5, 6} Therefore, the increase of curvature energy hinders further membrane wrapping (Fig. 2C).

Full Wrapping. We then gradually decreased the interaction parameter $a_{H_T H_M}$ from 10.0 to 0.0 at $\rho_{LNPA} = 1.4$. Note that decreasing $a_{H_T H_M}$ corresponds to the increase of tube-membrane adhesion strength. The time evolutions of wrapping percentage under different values of $a_{H_T H_M}$ are shown in Fig. 3A, which demonstrates that the

membrane wrapping efficiency is significantly promoted by increasing tube-membrane adhesion strength. When $a_{H_T H_M} > 4.0$, the wrapping percentage achieved low values rapidly and kept nearly unchanged in the rest simulation time. Final configurations show that the tubes were only partially wrapped by the membranes (Fig. 3B). When $a_{H_T H_M} < 4.0$, however, the wrapping dynamics is different. After a rapid increase of wrapping percentage, the wrapping proceeded until the tube was fully wrapped. Here, we should note that the wrapping percentage was calculated by dividing the lipid number contacting with membrane by that of the whole tube. Considering that the inner lipid molecules never contact with the membrane, the calculated percentage for full wrapping is thus not equal to 1.0 but approximately the ratio of outer to whole lipid number.

Now we give the detailed pathway of full wrapping under the condition of $a_{H_T H_M} = 0.0$. According to the time evolution of wrapping percentage (Fig. 3), the whole wrapping process can be divided into three stages. The first stage is featured by a rapid increase of the wrapping percentage ($0 < t < 50000$). The rapid wrapping is due to the membrane bending as a normal endocytic pathway (Fig. 4A). At the same time, the cylindrical tube was deformed into an oblate shape, as reflected by evolution of the ellipsoidal ratio (Fig. 4B). The tube deformation further increases the tube-membrane adhesion area but also induces simultaneously the increases of the local curvature nearby the contact line. For weak tube-membrane adhesion, the higher extent of wrapping is hindered by the increase of local curvature (Fig. 2). For rigid NPs, the high membrane bending energy can be overcome by passive NP rotation^{28, 49} or NP clustering.^{24, 25, 50} For soft cylindrical tubes under strong tube-membrane adhesion, however, the subsequent wrapping still proceeded via following responses ($50000 < t < 300000$). Firstly, the deformed tube gradually changed its shape and the high local curvature was accordingly reduced (Fig. 4B). Secondly, the upper leaflet of the membrane around the wrapping front started to protrude and wrapped the tube from the top side (Fig. 4A). To illustrate the detailed structure of protrusion, we provide the sectional view in Figure S1. It clearly shows that after initiation from

upper leaflet, the protrusion quickly forms bilayer and grows along the tube surface. Once the protrusion is initiated the wrapping process does not terminate until the full wrapping is reached. Therefore, the late tube wrapping by membrane is mainly accomplished via membrane monolayer protrusion. Here, we should distinguish monolayer protrusion from bilayer protrusion. Specifically, bilayer protrusion is to describe the severe membrane deformation, which can play role in the coupled cell adhesion.⁵¹ Besides, cell entry of viruses was found to be accomplished via bilayer protrusion, the growth of which finally develops to the macropinocytosis.⁵² Comparatively, the monolayer protrusion is much more localized and usually initiates from the upper membrane leaflet.

Heterogeneous Wrapping Dynamics. Although cylindrical tubes are finally wrapped by membranes homogeneously, the wrapping dynamics is apparently heterogeneous along the tube axial direction (Fig. 4A, Video S1). To analyze the wrapping dynamics, the whole tube was divided into four short segments. The evolutions of both local tube radius and local wrapping percentage for each segment were then calculated (Fig. 5). Clearly, the tube underwent a heterogeneous deformation as the wrapping proceeds (Fig. 5A, B). After a short initial increase of the tube radius ($t < 40000$), two tube segments started to shrink (Fig. 5A, $40000 < t < 125000$), while the other segments continued to expand (Fig. 5B, $t < 125000$). According to the typical snapshot and evolution of local wrapping percentage, the wrapping of four tube segments is apparently asynchronous (Fig. 5C). In other words, the wrapping of two shrinking tube segments first completes, while that of the other two expanding segment lags behind. Once the local wrapping completes via monolayer protrusion, the local tube radius turns to increase while the other two segments start to shrink and accordingly complete the local wrapping (Fig. 5, $t > 125000$).

In fact, we have performed five more independent simulations starting from the same initial configuration but with different initial velocity distributions. Interestingly, all five simulations show heterogeneous wrapping dynamics (Fig. S2). We ascribe the heterogeneous wrapping dynamics to the cooperation between tube deformation and

monolayer protrusion. Besides membrane bending, the first increase of tube-membrane contact area is mainly accomplished via tube deformation. As a consequent, the local tube curvature increases and thus hinders the membrane bending to wrap tube in a higher extent. The other effect is to increase the tube surface tension.⁴¹ The increased tube tension is then released by a slight local tube shrinkage, which is marked by arrows in Figure 4A at $t = 50000$. Once the shrinkage is initiated, the upper lipid monolayer starts to protrude and wraps the local tube from the top side (arrows in Fig. 4A, $t = 80000$). After the local wrapping completes, the shrinking tube segments turn to expand to initiate the wrapping of other tube segments (Fig. 5C). Finally, the tube turns back to be cylindrical and be wrapped by the membrane homogeneously (Fig. 4A, $t = 500000$).

3.2 Tube-membrane Adhesion Affects Tube Pearling

Our simulations show that the tube-membrane adhesion may result in tube pearling. Thus for designing tubular polymersomes for drug delivery, the tube pearling should be taken into account because it affects the internalization kinetics and even alters the subsequent fate. In vitro, the tube pearling can be somewhat modulated by altering lipid components.³⁵ For example, cholesterol increases the membrane bending rigidity and thus prevents their pearling transition.⁵³ Nevertheless, under external interventions, like polymer anchorage and electric field, the high bending energy can be overcome and thus leads to the tube pearling.^{48, 54} Here, we want to answer the following question: How does tube-membrane adhesion affect tube pearling?

Weak Tube-membrane Adhesion Drives Tube Pearling. First, we fixed $a_{H_r H_M} = 10.0$ and $\rho_{LNPA} = 1.2$, which represent weak tube-membrane adhesion strength and highly positive membrane tension, respectively. Our simulations show that under such conditions, a finite extent of tube pearling could take place on the membrane surface (Fig. S3A). In more detail, the tube first underwent a finite deformation to increase

the tube-membrane contact area. The tube deformation can be reflected by a striking increase of the tube surface area (Fig. S3B). As the number of lipids forming the tube was fixed, the increased tube surface area thus corresponds to an increase of the tube surface tension. To release the tension, a finite tube pearling was initiated (Fig. S3A, $t = 75000$). Meanwhile, the tube surface area gradually decreased as the pearling proceeds (Fig. S3B, $t > 75000$).

Strong Tube-membrane Adhesion Restrains Tube Pearling. Different from that weak tube-membrane adhesion drives tube pearling, our simulations clearly show that in the case of strong tube-membrane adhesion, tubes significantly wrapped by the membrane could not undergo pearling (Figs. 2-4). In this part, in order to accelerate tube pearling we artificially transferred a number of water beads from outside to inside.⁴⁵ Then the tube-membrane interaction parameter $a_{H_T H_M}$ was varied to explore its effect on tube pearling.

First, for the situation of $\rho_{LNPA} = 1.5$ and $a_{H_T H_M} = 12.0$, our simulation shows that the tube undergoes a thorough pearling on the membrane surface (Fig. 6 and Video S2). Namely, the cylindrical tube is gradually divided into two vesicles, which are connected by a short cylindrical micelle (Fig. 6A). The pearling dynamics is well reflected by the evolution of the local tube radius, which show that two adjacent segments undergo shrinking and expanding, respectively (Fig. 6B). Besides, we calculated the local wrapping percentages of the two segments (Fig. 6C). Clearly, the local tube shrinkage is accompanied by a striking increase of the local wrapping percentage. Comparatively, the wrapping extent of the expanding tube segment keeps nearly unchanged.

Next, we fixed $\rho_{LNPA} = 1.5$ and gradually increased $a_{H_T H_M}$. Our simulations show that thorough tube pearling takes place for the weak tube-membrane adhesion (Fig. 6). As we decreased $a_{H_T H_M}$ from 12.0 to 10.0, the wrapping efficiency increased as expected, but only partial tube pearling was found (Fig. S4A). When $a_{H_T H_M} = 8.0$, no

obvious tube pearling was observed, although the tube was wrapped partially by the membrane (Fig. S4B). As we further decreased $a_{H_T H_M}$ to 0.0, the tube was finally wrapped by the membrane completely. Meanwhile, no pearling takes place during the wrapping process (Fig. S4C).

For individual tubes, it has been demonstrated both experimentally and theoretically that tube pearling could be induced by increasing tension of membrane tubes.⁵⁵ For tubes being wrapped by membranes, however, our simulations here show a different pearling mechanism. This is because the pearling of a tube being wrapped by a flat membrane certainly causes the bending of the membrane with the same curvature. In other words, during the pearling process the increase of tube tension must compete with the increase of the curvature energy for both the tube and the curved membrane. Therefore, once a tube is highly wrapped by a membrane the tube pearling will be effectively restrained since it would cause a sharp increase of the membrane bending energy.

Besides the tube-membrane adhesion strength, the wrapping efficiency and pearling instability are also affected by the membrane surface tension. Our extensive simulations indicate that four different equilibrium configurations are observed through varying both ρ_{LNPA} and $a_{H_T H_M}$ (see the phase diagram in Fig. 7). They are thorough tube pearling with partial membrane wrapping, partial tube pearling with partial membrane wrapping, partial membrane wrapping without tube pearling, and full membrane wrapping without tube pearling, respectively.

As discussed above, the final tube pearling instability is restrained by significant membrane wrapping. Dynamically, whether tube pearling occurs or not is determined by comparing the pearling time with the membrane wrapping time. When the membrane tension is highly positive (for example, $\rho_{LNPA} = 1.2$), the membrane wrapping is strongly restrained and thus tube pearling takes place under both strong and weak tube-membrane adhesions. Under intermediate membrane tension (for example, $\rho_{LNPA} = 1.5$), the wrapping efficiency can be either high or low, depending

on the tube-membrane adhesion strength. Once a certain part of tube is wrapped by membrane before the onset of pearling, the subsequent tube pearling will be prevented. Therefore, partial pearling or even no pearling can take place. When the membrane tension is highly negative, the membrane wrapping can proceed without a high membrane bending penalty to overcome. In this situation, the tube pearling is restrained by membrane wrapping.

3.3 Membrane Wrapping of Pearled Tubes

In the above section, we explored how tube-membrane adhesion affects tube pearling. Here, we concentrated on the opposite case, namely, how pearled tubes interact with membranes. For individual tubes, different levels of pearling might take place under external interventions, like polymer anchorage and electric field.^{48, 54} Therefore, it is equally important to understand how the pearled tubes interact with membranes. To this end, we extracted the final configuration of tube pearling under $\rho_{LNPA} = 1.4$ and $a_{H_T H_M} = 12.0$ (Fig. 6) as the initial structure for further wrapping. In the subsequent simulations, we fixed the membrane tension but artificially increased the tube-membrane adhesion strength by decreasing $a_{H_T H_M}$ from 12.0 to 0.0. In reality, the increase of NP-membrane adhesion strength can be realized by quick adsorption of certain molecules on the NP surface that forms protein corona.⁵⁶

The membrane wrapping process of one pearled tube is given in Figure S5 and Video S3. With the increase of the tube-membrane adhesion strength, the pearled tube was found to be wrapped by membrane more efficiently. On one hand, the membrane undergoes a strong deformation to wrap the tube as in an endocytic pathway. On the other hand, the monolayer protrusion is initiated at the wrapping front and preferentially wraps the vesicle region rather than the micelle region. As the wrapping proceeds, more lipid molecules diffuse from the tube to contact with membrane, which further increase the local tube tension. As a result, the pearled tube further undergoes the pearling division, and finally, the pearled tube is completely wrapped by the membrane.

3.4 Membrane Fusion Promotes Tube Pearling

Besides membrane wrapping, the other interaction pathway is the tube-membrane fusion. For vesicles, it has been known that membrane fusion could alter the tension of vesicles.⁴¹ Similarly, for cylindrical tubes we speculated that tube pearling, which is driven by tension, is also affected by the tube-membrane fusion. In reality, membrane fusion can be promoted by introduction of specific proteins, like SNARE proteins.⁵⁷ Contrarily, by anchoring other proteins, like α -synuclein and β -amyloid, on the vesicle surface, the membrane fusion can be effectively blocked.⁵⁸ Here, for simplicity we artificially altered the interaction parameter a_{TTM} from 200.0 to 25.0 to permit tube-membrane fusion, while a_{HTM} was fixed to 2.0. Three different values of ρ_{LNPA} , including 1.2, 1.3 and 1.4, were applied to consider the effect of membrane tension.

First, we set the lipid density to $\rho_{LNPA} = 1.2$, which represents highly positive membrane tension. After a short tube-membrane adhesion, the onset of tube-membrane fusion first takes place at the place of the contact line with a high curvature (Fig. 8A, $t = 20000$). This is because the membrane fusion is initiated by lipid tail protrusion, which is enhanced for highly curved system, consistent with previous studies.⁵⁹ For example, both MD and DPD simulations suggested that the vesicle fusion occurs initially at the places of high curvature.^{60, 61} Our simulation results indicate that once the fusion is initiated, more lipid molecules gradually diffuse from tube to mix with the membrane. In contrast, the opposite lipid diffusion from membrane to tube is less pronounced because of the highly positive membrane tension. The one-way (asymmetric) lipid diffusion between tube and membrane increases the tube tension and thus leads to the subsequent pearling transition.

Next, we decreased the membrane tension by increasing ρ_{LNPA} from 1.2 to 1.3. As a consequent, the membrane wrapping efficiency increased (Fig. 8B). Besides, no membrane fusion at the early stage was observed until the membrane monolayer

protrusion was initiated (Fig. 8B, $t = 250000$). As the edge of membrane protrusion has a much higher curvature, lipid molecules first diffused from the protrusion to mix with the tube. Similar to the case of $\rho_{LNPA} = 1.2$, the directed lipid diffusion from tube to membrane was observed again but restrained by the decrease of membrane tension. As a result, the increase of tube tension is less obvious and only partial pearling finally takes place.

At last, we fixed the lipid density ρ_{LNPA} to 1.4, which represents near zero membrane surface tension. As expected, the early membrane wrapping was highly promoted. Besides, the tube-membrane fusion was also initiated via lipid diffusion from the monolayer protrusion to the tube (Fig. 8C, $t = 150000$). Nevertheless, under near zero membrane tension, the lipid diffusion between tube and membrane is almost symmetric, i.e., a two-way diffusion. Therefore, the tube surface tension keeps nearly unchanged. Finally, the lipids of tube and membrane were completely mixed and no pearling takes place (Fig. 8D).

4. Conclusions

Compared with traditional rigid NPs, soft elastic NPs, like vesicles and polymersomes, offer particular advantages in biomedical applications, such as high solubility, high environmental sensitivity, biocompatibility and low toxicity. Interestingly, recent experimental studies found that tubular polymersomes display different cellular internalization kinetics compared with spherical ones, underlying the molecular mechanism that is not fully understood.³⁵ On the other hand, a fundamental question regarding the formation of the membrane tube bridging two eukaryotic cells for intercellular material exchange and signal communication, namely how a membrane tube initiated from a cell interacts with the membrane of another cell, remains unsolved. To illustrate the questions, in this work, we have applied the DPD simulation method to systematically investigate the interaction between cylindrical tubes and biomembranes. Depending on the tube-membrane adhesion strength and membrane surface tension, three different interaction pathways have been identified.

They are membrane wrapping, tube-membrane fusion and tube pearling, respectively.

First, our extensive simulations indicate that soft tubes can be wrapped by membranes. Unlike spherical vesicles, the wrapping of cylindrical tubes is accomplished via membrane monolayer protrusion, which wraps the tube from the top side. Besides, the monolayer protrusion and tube deformation cooperatively make the wrapping dynamics heterogeneous along tube axial direction. This observation may explain the experimental observation that tubular polymersomes have different cellular internalization kinetics compared with spherical ones. Our simulations also suggest that cylindrical tubes undergo different pearling transitions on the membrane surface, depending on the tube-membrane adhesion. The weak tube-membrane adhesion is found to promote tube pearling, while the strong tube-membrane adhesion induces significant membrane wrapping that contrarily prevents the pearling.

Besides membrane wrapping, cylindrical tubes can fuse with membranes. Depending on the membrane surface tension, the lipid diffusion between tubes and membranes can be symmetric or asymmetric. Especially, under highly positive membrane tension, more lipid molecules diffuse from tubes to membranes, which leads to the increase of tube tension and promotes tube pearling.

Acknowledge

This work is financially supported by National Natural Science foundation of China (No. 21303269, 21273287), Natural Science foundation of Shandong Province (ZR2013BQ029) and the Qingdao Science and Technology Project (No. 13-1-4-235-jch). The authors thank the National Supercomputing Center in Shenzhen for providing excellent computer time.

References

1. T. L. Doane and C. Burda, *Chem. Soc. Rev.*, 2012, **41**, 2885-2911.
2. D. Peer, J. M. Karp, S. Hong, O. C. Farokhzad, R. Margalit and R. Langer, *Nat. Nanotechnol.*, 2007, **2**, 751-760.
3. N. L. Rosi and C. A. Mirkin, *Chem. Rev.*, 2005, **105**, 1547-1562.
4. S. Jiang, K. Y. Win, S. Liu, C. P. Teng, Y. Zheng and M. Y. Han, *Nanoscale*, 2013, **5**, 3127-3148.

5. M. Deserno, *Phys. Rev. E*, 2004, **69**, 031903.
6. H. J. Gao, W. D. Shi and L. B. Freund, *Proc. Natl. Acad. Sci. U. S. A.*, 2005, **102**, 9469-9474.
7. E. M. Curtis, A. H. Bahrami, T. R. Weikl and C. K. Hall, *Nanoscale*, 2015, **7**, 14505-14514.
8. K. Yang and Y. Q. Ma, *Nat. Nanotechnol.*, 2010, **5**, 579-583.
9. X. Yi, X. Shi and H. Gao, *Nano Lett.*, 2014, **14**, 1049-1055.
10. Y. Li, T. Yue, K. Yang and X. Zhang, *Biomaterials*, 2012, **33**, 4965-4973.
11. T. Yue, X. Wang, F. Huang and X. Zhang, *Nanoscale*, 2013, **5**, 9888-9896.
12. S. Dasgupta, T. Auth and G. Gompper, *Nano Lett.*, 2014, **14**, 687-693.
13. R. Vacha, F. J. Martinez-Veracoechea and D. Frenkel, *Nano Lett.*, 2011, **11**, 5391-5395.
14. X. Yi, X. Shi and H. Gao, *Phys. Rev. Lett.*, 2011, **107**, 098101.
15. T. Yue and X. Zhang, *Soft Matter*, 2013, **9**, 559-569.
16. X. Yi and H. Gao, *Soft Matter*, 2015, **11**, 1107-1115.
17. Y. Li, X. Zhang and D. Cao, *Nanoscale*, 2015, **7**, 2758-2769.
18. J. Sun, L. Zhang, J. Wang, Q. Feng, D. Liu, Q. Yin, D. Xu, Y. Wei, B. Ding, X. Shi and X. Jiang, *Adv. Mater.*, 2015, **27**, 1402-1407.
19. R. C. Van Lehn, M. Ricci, P. H. J. Silva, P. Andreozzi, J. Reguera, K. Voitchovsky, F. Stellacci and A. Alexander-Katz, *Nat. Comm.*, 2014, **5**, 4482.
20. H. M. Ding, W. D. Tian and Y. Q. Ma, *Acs Nano*, 2012, **6**, 1230-1238.
21. H. M. Ding and Y. Q. Ma, *Biomaterials*, 2012, **33**, 5798-5802.
22. H. M. Ding and Y. Q. Ma, *Small*, 2015, **11**, 1055-1071.
23. S. Zhang, H. Gao and G. Bao, *Acs Nano*, 2015, **9**, 8655-8671.
24. T. Yue and X. Zhang, *Acs Nano*, 2012, **6**, 3196-3205.
25. K. Jaskiewicz, A. Larsen, D. Schaeffel, K. Koynov, I. Lieberwirth, G. Fytas, K. Landfester and A. Kroeger, *Acs Nano*, 2012, **6**, 7254-7262.
26. M. Raatz, R. Lipowsky and T. R. Weikl, *Soft Matter*, 2014, **10**, 3570-3577.
27. A. Saric and A. Cacciuto, *Phys. Rev. Lett.*, 2012, **109**, 188101.
28. C. Huang, Y. Zhang, H. Yuan, H. Gao and S. Zhang, *Nano Lett.*, 2013, **13**, 4546-4550.
29. E. Zhang, M. F. Kircher, M. Koch, L. Eliasson, S. N. Goldberg and E. Renstrom, *Acs Nano*, 2014, **8**, 3192-3201.
30. T. Yue, X. Zhang and F. Huang, *Soft Matter*, 2015, **11**, 456-465.
31. L. Zhang and X. Wang, *Nanoscale*, 2015, **7**, 13458-13467.
32. F. Meng, Z. Zhong and J. Feijen, *Biomacromolecules*, 2009, **10**, 197-209.
33. J. Z. Du and R. K. O'Reilly, *Soft Matter*, 2009, **5**, 3544-3561.
34. S. Li, K. Hu, W. Cao, Y. Sun, W. Sheng, F. Li, Y. Wu and X. J. Liang, *Nanoscale*, 2014, **6**, 13701-13709.
35. J. D. Robertson, G. Yealland, M. Avila-Olias, L. Chierico, O. Bandmann, S. A. Renshaw and G. Battaglia, *Acs Nano*, 2014, **8**, 4650-4661.
36. G. P. Dubey and S. Ben-Yehuda, *Cell*, 2011, **144**, 590-600.
37. M. Laradji and P. B. Sunil Kumar, *Phys. Rev. Lett.*, 2004, **93**, 198105.
38. P. J. Hoogerbrugge and J. M. V. A. Koelman, *Europhys. Lett.*, 1992, **19**, 155.
39. P. Español and P. Warren, *Europhys. Lett.*, 1995, **30**, 191.
40. R. D. Groot and P. B. Warren, *J. Chem. Phys.*, 1997, **107**, 4423.
41. J. C. Shillcock and R. Lipowsky, *Nat. Mater.*, 2005, **4**, 225-228.
42. R. Guo, J. Mao and L. T. Yan, *Acs Nano*, 2013, **7**, 10646-10653.

43. A. Alexeev, W. E. Uspal and A. C. Balazs, *Acs Nano*, 2008, **2**, 1117-1122.
44. N. Arai, K. Yasuoka and X. C. Zeng, *Nanoscale*, 2013, **5**, 9089-9100.
45. T. Yue, X. Zhang and F. Huang, *Phys. Chem. Chem. Phys.*, 2014, **16**, 10799-10809.
46. T. Yue, S. Li, X. Zhang and W. Wang, *Soft Matter*, 2010, **6**, 6109-6118.
47. H. Tang, H. Ye, H. Zhang and Y. Zheng, *Soft Matter*, 2015, DOI: 10.1039/C5SM01460C.
48. K. P. Sinha, S. Gadkari and R. M. Thaokar, *Soft Matter*, 2013, **9**, 7274-7293.
49. X. Shi, A. von dem Bussche, R. H. Hurt, A. B. Kane and H. Gao, *Nat Nanotechnol*, 2011, **6**, 714-719.
50. B. J. Reynwar, G. Illya, V. A. Harmandaris, M. M. Muller, K. Kremer and M. Deserno, *Nature*, 2007, **447**, 461-464.
51. K. A. DeMali and K. Burridge, *Journal of cell science*, 2003, **116**, 2389-2397.
52. J. Mercer and A. Helenius, *Nature cell biology*, 2009, **11**, 510-520.
53. S. Winzen, M. Bernhardt, D. Schaeffel, A. Koch, M. Kappl, K. Koynov, K. Landfester and A. Kroeger, *Soft Matter*, 2013, **9**, 5883-5890.
54. I. Tsafir, D. Sagi, T. Arzi, M. A. Guedeau-Boudeville, V. Frette, D. Kandel and J. Stavans, *Phys. Rev. Lett.*, 2001, **86**, 1138-1141.
55. R. Bar-Ziv and E. Moses, *Phys. Rev. Lett.*, 1994, **73**, 1392-1395.
56. H. M. Ding and Y. Q. Ma, *Biomaterials*, 2014, **35**, 8703-8710.
57. H. J. Risselada and H. Grubmuller, *Curr. Opin. Struc. Biol.*, 2012, **22**, 187-196.
58. B. K. Choi, J. Y. Kim, M. Y. Cha, I. Mook-Jung, Y. K. Shin and N. K. Lee, *Biochemistry-Us*, 2015, **54**, 1831-1840.
59. D. Mirjanian, A. N. Dickey, J. H. Hoh, T. B. Woolf and M. J. Stevens, *J. Phys. Chem. B*, 2010, **114**, 11061-11068.
60. S. J. Marrink and A. E. Mark, *J. Am. Chem. Soc.*, 2003, **125**, 11144-11145.
61. A. Grafmuller, J. Shillcock and R. Lipowsky, *Biophys. J.*, 2009, **96**, 2658-2675.

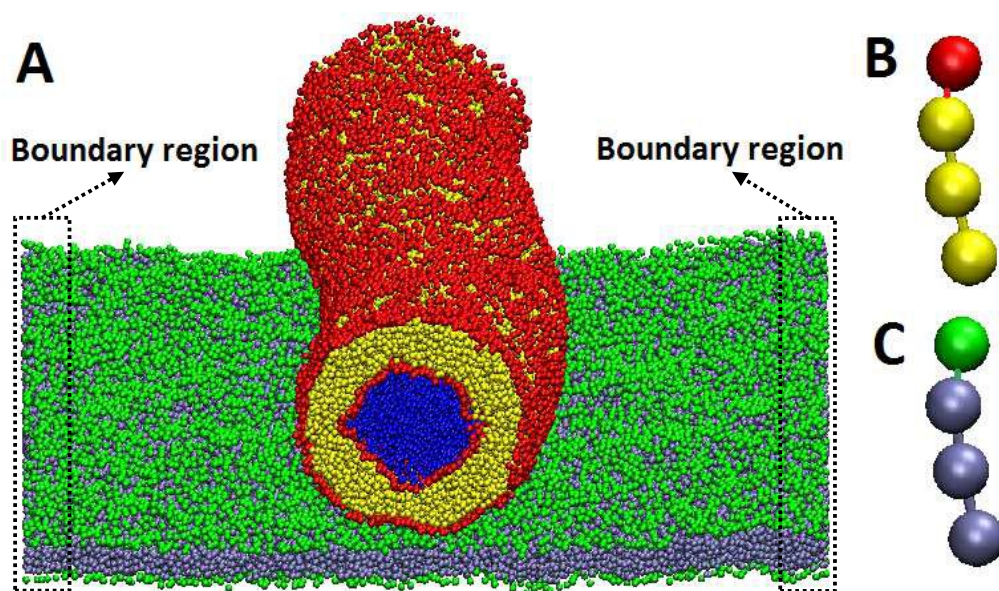


Fig. 1 Schematic representation of the interaction between tube and membrane. Lipid head and tail of the tube are shown in red and yellow, while those of the membrane are shown in green and iceblue. The water beads inside the tube are shown in blue, while those outside the tube are not shown for clarity. Two boundary regions in which lipids are added or deleted according to the membrane tension are marked in both sides of the tube.

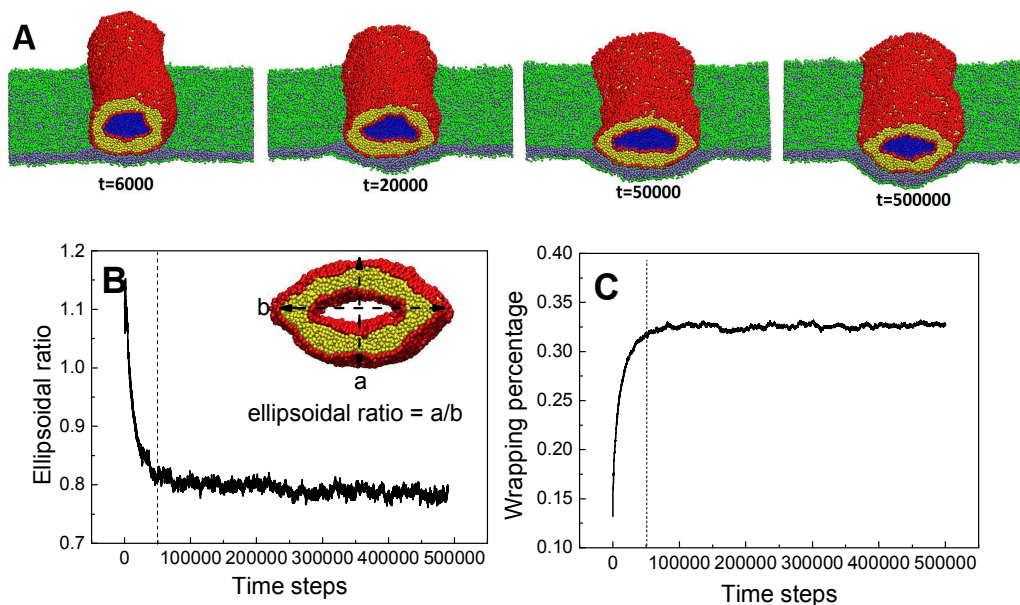


Fig. 2 Slight partial wrapping of tube by membrane under weak tube-membrane adhesion strength ($a_{H_T H_M} = 10.0$). A shows the typical snapshots, B shows the time evolution of ellipsoidal ratio of tube during wrapping process, and C shows the evolution of wrapping percentage of tube by membrane. The value of ρ_{LNPA} is set to 1.4, which represents near zero membrane surface tension. The inset shows the definition of ellipsoidal ratio of the tube.

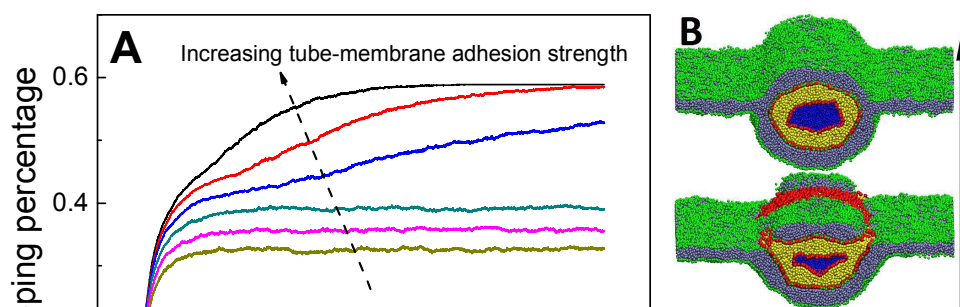


Fig. 3 Effect of tube-membrane adhesions strength on membrane wrapping dynamics. A shows the time evolution of wrapping percentage under different tube-membrane adhesion strength. B shows the final configurations under different tube-membrane interaction parameters ($a_{H_r H_M} = 8.0, 4.0$ and 0.0 , from bottom to top). The value of ρ_{LNPA} representing the membrane tension is fixed to 1.4.

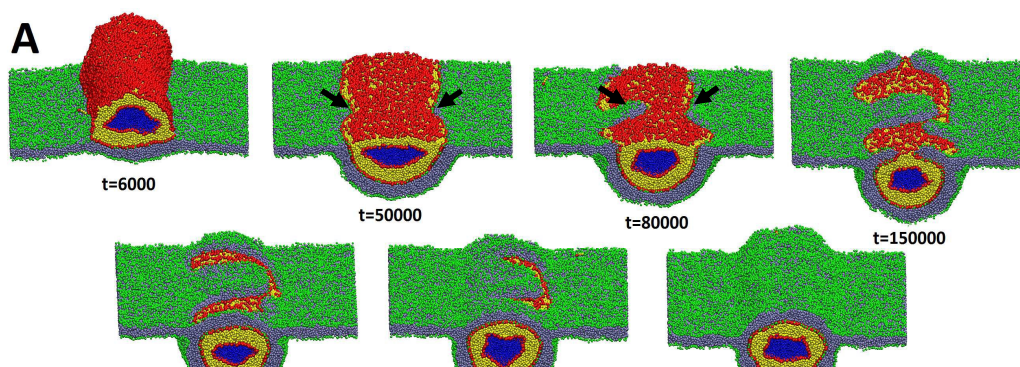


Fig. 4 Full wrapping dynamics of tube by membrane under strong tube-membrane adhesion strength ($a_{H_T H_M} = 0.0$). The tube deformation is illustrated in the evolution of tube ellipsoidal ratio during the wrapping process. The inset gives the typical snapshots showing the transient tube morphology. The defined lipid density is set to $\rho_{LNPA} = 1.4$. The black arrows highlight the local slight tube shrinkage, which initiates the subsequent monolayer protrusion.

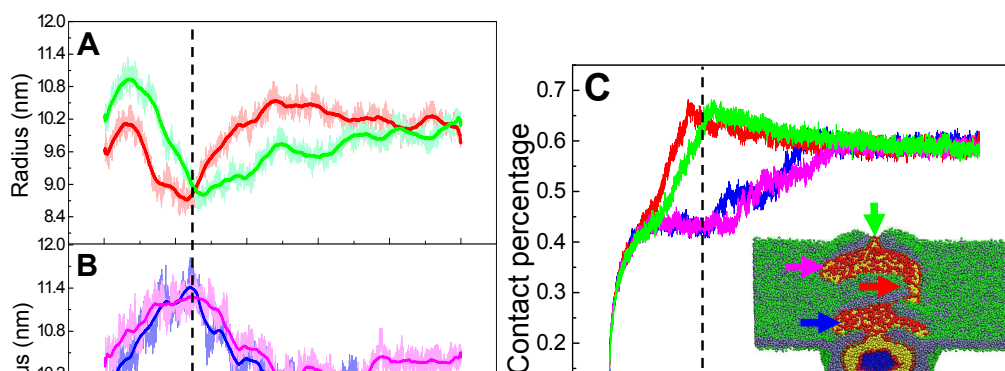


Fig. 5 Heterogeneous wrapping dynamics along tube axial direction. A and B show the time evolutions of local tube radius, C shows the evolution of local wrapping percentage. The inset shows the snapshot of instantaneous wrapping state at $t = 125000$ steps.

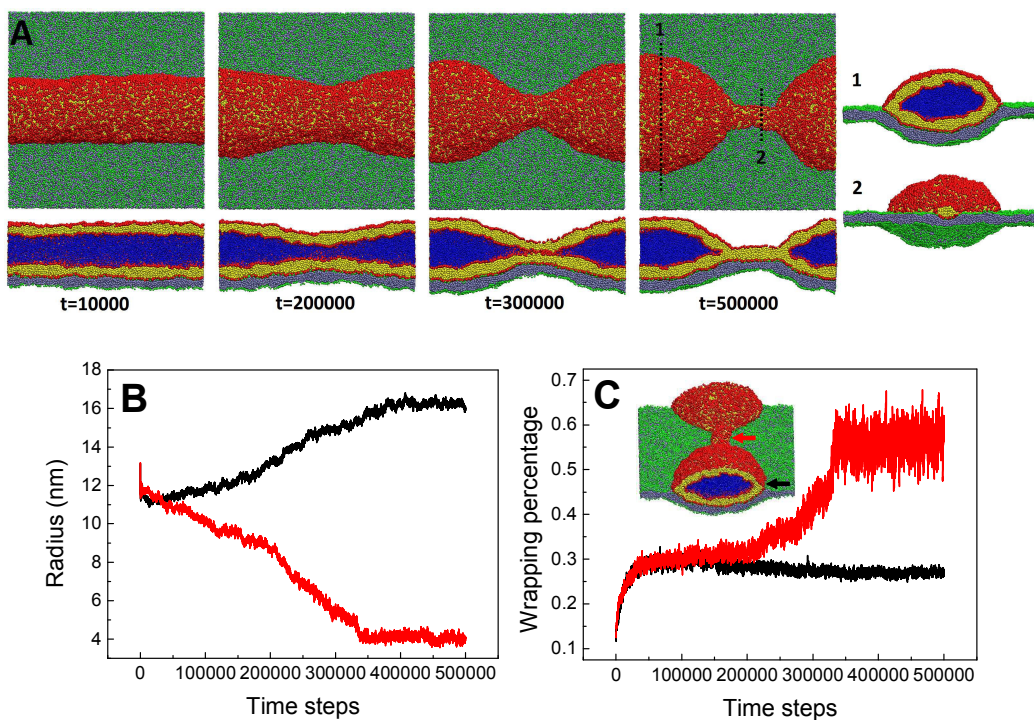


Fig. 6 Thorough tube pearling on the membrane surface. A shows the typical snapshots, B shows the evolution of local tube radius, C shows the evolution of local wrapping percentage. The tube-membrane interaction parameter is set to $a_{H_T H_M} = 12$, the lipid density is set to $\rho_{LNPA} = 1.4$.

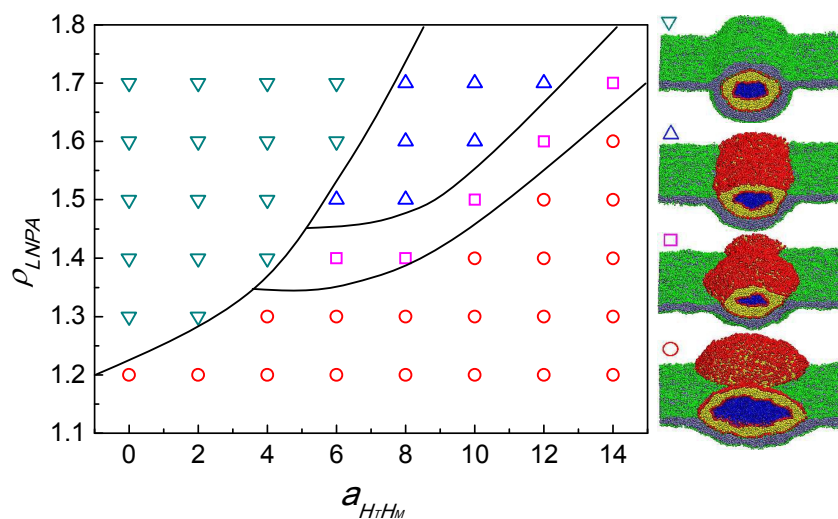


Fig. 7 Phase diagram as a function of tube-membrane interaction parameter ($a_{H_T H_M}$) and lipid density (ρ_{LNPA}) showing different extent of membrane wrapping and tube pearling. ∇ represents no tube pearling combined with full membrane wrapping; \triangle represents no tube pearling combined with partial membrane wrapping; \square represents partial tube pearling combined with partial membrane wrapping; and \circ represents thorough tube pearling combined with partial membrane wrapping.

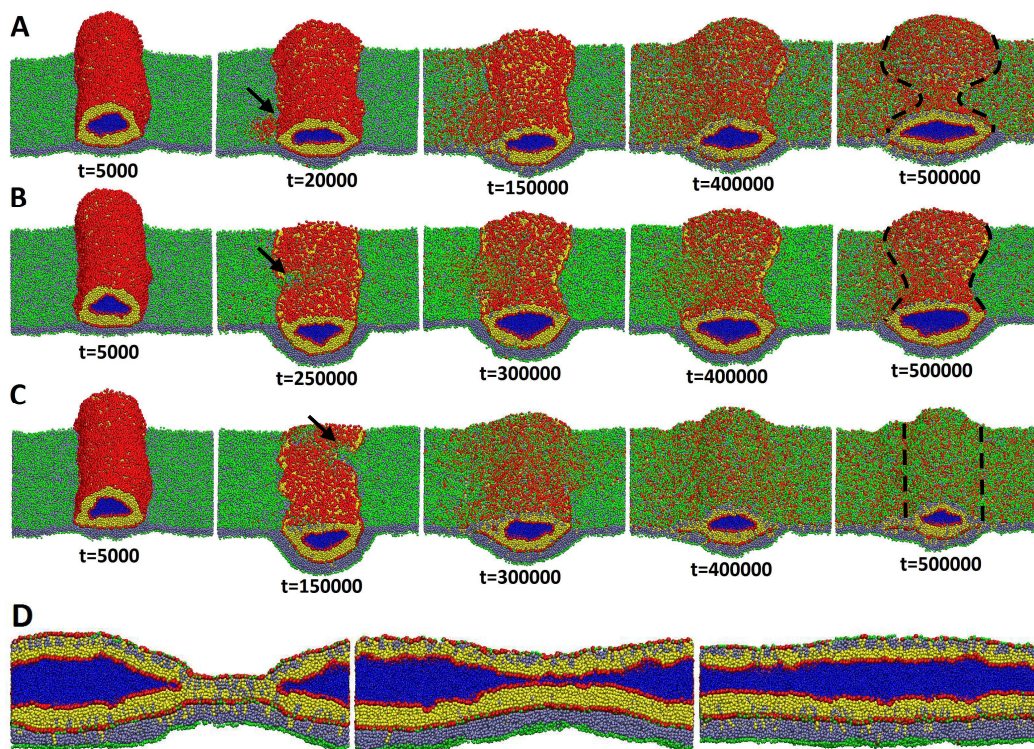


Fig. 8 Tube-membrane fusion under different membrane tension. The tube-membrane interaction parameter is set to $a_{H_T H_M} = 2.0$. Three values of lipid density are applied, including $\rho_{LNP A} = 1.2$ (A), $\rho_{LNP A} = 1.4$ (B), and $\rho_{LNP A} = 1.5$ (C), respectively. D shows the cross section of tube-membrane system under each tension. The initiation of tube-membrane fusion is labeled by three black arrows. The final pearling outline is strengthened by dashed curves.